# Measurement of the x-ray mass attenuation coefficient and the imaginary part of the form factor of silicon using synchrotron radiation

C. Q. Tran, C. T. Chantler, and Z. Barnea
*School of Physics, University of Melbourne, Victoria 3010, Australia*

D. Paterson
*SRI-CAT, APS, Argonne National Laboratory, 9700 South Cass Avenue, Argonne, Illinois 60439*

D. J. Cookson
*ANSTO, Private Mail Bag 1, Menai, New South Wales 2234, Australia*
*and Chem-Mat-CARS-CAT (Sector 15, Building 434D), Argonne National Laboratory, 9700 South Cass Avenue, Argonne, Illinois 6043*
(Received 10 December 2002; published 28 April 2003)

We used the x-ray extended-range technique to measure the x-ray mass attenuation coefficients of silicon with an accuracy between 0.27% and 0.5% in the 5 keV−20 keV energy range. Subtraction of the x-ray scattering contribution enabled us to derive the corresponding x-ray photoelectric absorption coefficients and determine the absolute value of the imaginary part of the atomic form factor of silicon. Discrepancies between the experimental values of the mass attenuation coefficients and theoretically calculated values are discussed. New approaches to the theoretical calculation will be required to match the precision and accuracy of the experimental results.

DOI: 10.1103/PhysRevA.67.042716 PACS number(s): 32.80.Cy, 78.20.Ci, 78.70.Dm, 78.20.Bh

## I. INTRODUCTION

The integration density of silicon-based chips has doubled every 12–18 months as a result of the continuously improved techniques of characterization and fabrication of this material [1]. Crystalline silicon is among the most perfect of crystalline materials whose lattice structure has been characterized to the highest accuracy for use as a standard reference crystal [$d(220)=0.192\,015\,570(6)\times10^{-9}$ m, [2,3]] and standard powder sample (Si640b $a_0=5.430\,940(11)$ Å [4], equivalent to 2 ppm accuracy). Frontier applications of silicon include biosensors [5], solar cells [6], x-ray crystal resonators [7], quantum computing [8], and many more. The current rate of miniaturization of silicon-based chip manufacturing, together with the exploration of the idea of silicon quantum computers has rapidly increased the demand for detailed knowledge of silicon at atomic and macroscopic levels.

The complex x-ray form factor $f$ for a given atom, element, or solid is the resonant scattering amplitude of x rays due to the charge distribution, which determines refractive indices, scattering, and attenuation coefficients and hence critical properties for x-ray optical devices, for x-ray topography, lithography, and general synchrotron investigations.

Although many users assume that the form factor and individual cross-sections of silicon are accurately known, unfortunately, significant disagreements between theoretical and experimental results remain in the literature. In fact, theoretical predictions of the atomic form factor and individual cross-sections of silicon are not better known than those of other less tested elements. Figure 1 shows a comparison between two commonly used theoretical predictions of the mass attenuation coefficient of silicon between 5 keV–50 keV and corresponding experimental measurements prior to the investigation reported here.

From Fig. 1 the mass attenuation coefficients of the two theories are seen to disagree by up to 5%. Below 30 keV, the discrepancy in the (total) mass attenuation coefficients is caused mainly by the uncertainty in the photoelectric cross-sections. In this energy range, contributions from scattering (Compton and thermal diffuse) are insignificant at the level of the discrepancy of 5%.

Above 30 keV, contributions from scattering become increasingly significant. We note that, above 30 keV, various

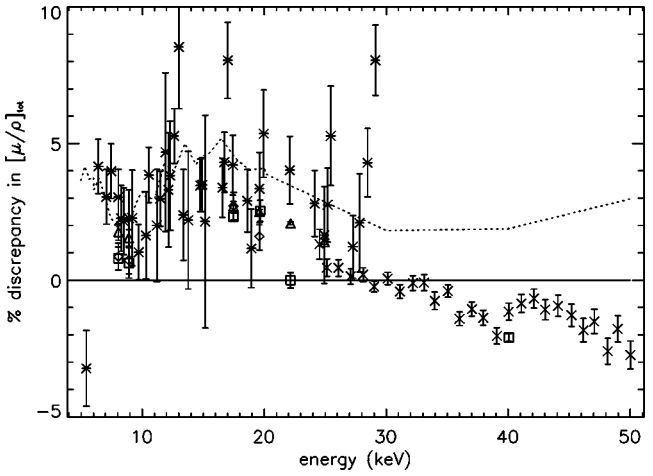


FIG. 1. Discrepancies in mass attenuation coefficients for silicon between experiments of Gerward [10] (diamond), Creagh and coworkers [11,12] (square), Mika *et al.* [13] (cross), Wang *et al.* [14] (asterisk), and Baltazar-Rodrigues and Cusatis [15] (triangle) and theory from Scofield [17,18] (dotted line) compared with Chantler [16] (solid line). Experimental data appear to favor Chantler's theory in the energy range above 25 keV. Below 16 keV, experimental data appear to favor the predictions of Scofield. Between 16 and 25 keV, experimental data are unable to address the 2–5% discrepancy between theoretical predictions.

 

predictions of the Rayleigh (for noncrystalline silicon) and thermal-diffuse scattering (TDS, for crystalline silicon) have large fractional discrepancies (11% and more than 15%, respectively). Their contribution to the total mass attenuation coefficients is, of course, smaller and depends, as will be discussed below, on the energy. However, addressing these discrepancies and alternative mechanisms for coherent scattering with high accuracy experiments is difficult, particularly using an approach based on attenuation measurement. The only evidence for a particular scattering model in this region is due to Ref. [9].

Major previous experimental work includes those from Gerward [10], Creagh and co-worker [11,12], Mika *et al.* [13], Wang *et al.* [14], and Baltazar-Rodrigues and Cusatis [15]. In the energy region above 25 keV, the experimental data of Fig. 1 appear to favor the theory of Chantler [16]. Below 16 keV, the theory of Scofield *et al.* [17,18] appears to agree better with experiment, but most experimental error bars are quite large and do not discriminate between these two calculations. Between 16 keV and 25 keV, it is unclear which of the two theories is more reliable. Since only a small number of precision experimental data are available below 25 keV, the theoretical discrepancy cannot be systematically addressed. There is also a fundamental question of why experimental results should agree with different theories within different energy ranges.

This investigation aims to obtain a high quality and extensive set of data to test the agreement of experimental measurements and the two theoretical predictions in the energy range between 5 keV and 20 keV. The experiments employed the x-ray extended-range technique (XERT) discussed earlier in the context of its application to copper [19–21].

In this paper, we shall describe the experimental setup and discuss in detail the data analysis and interpretation. The success of this will have implications for the accuracy of earlier experimental techniques and experimental results. Problems relating to the discrepancies between theoretical calculations, theoretical structures, and the validity of theoretical predictions of the photoelectric, Compton, and thermal-diffuse scattering components will be discussed.

## II. EXPERIMENTAL GEOMETRY

The schematic diagram of the experimental setup for the silicon measurements was almost identical to that in the copper measurements (Ref. [20], Fig. 1). At each energy we used three specimens of different thickness within the attenuation range of $0.5<\ln(I_0/I)<5$, where $I_0$ and $I$ are the incident and the attenuated intensities, respectively. The specimens used were in the form of thin single-crystal wafers, obtained from three sources: from the set of specimens used in the IUCr project [11,12], from those used in previous measurements of one of our collaborators [13], and from Stevenson, Division of Manufacturing Science & Technology, CSIRO. The thicknesses of the wafers ranged from 50 $\mu$m to 4 mm. The surface areas of these wafers were about $15\times 15$ mm$^2$. The [111] direction was nominally perpendicular to the wafer surface. The impurity levels of the wafers were insignificant.

Ten measurements were carried out for each wafer at each energy. Energies were stepped through from 5 keV to 12 keV monotonically in step sizes of 100 eV. Step sizes of 150 eV were used between 12 keV and 15 keV, and step sizes of 200 eV were used between 15 keV and 20 keV. Multiple specimens and repeated measurements were used to test the statistical precision of the measurements and to optimize the measurements. This also enabled careful studies of systematic contributions (harmonics, scattering, and detector linearity) which are impossible to quantify in measurements using a single specimen [20,21]. Further descriptions of the experimental setup and procedures as well as further details of this technique have been given elsewhere [20,21].

## III. SPECIMEN THICKNESS AND UNIFORMITY

A combination of methods was employed to determine the specimen thickness at the point of incidence of the x-ray beam in a procedure similar to that described in Refs. [19,20]. The procedure consisted of the following points.

(1) Obtaining the average thickness of the thickest specimen by weighing and carefully determining its area.

(2) Mapping the thickness of the specimen using a micrometer.

(3) Mapping the relative thickness of the central part of the specimen using x rays.

(4) Combining the results of the above three measurements and hence determining the average thickness of the $1\times 1$ mm$^2$ area through which the x-ray beam actually passed during the attenuation measurement.

(5) Relating the thicknesses of all other specimens to the absolute thickness of the thickest specimen by measuring their relative absorption of x rays at one or more energies.

### A. Application to the thickest 4-mm specimen

#### *1. Average thickness by weighing of known area*

The average thickness $t_{ave}$ of the entire specimen was determined from $t_{av}=M/\rho A$ in which the mass $M$ and surface area $A$ were measured using the apparatus discussed in Ref [20]. The results were $M=(2.01226\pm 0.00001)$ g (i.e., $\pm 0.0005\%$) and $A=(221.582\pm 0.106)$ mm$^2$ (i.e., $\pm 0.048\%$). The surface $A$ was the average of the areas of the two surfaces of the crystal. The density $\rho$ used was 2.32 904(2) g/cm$^3$ using NIST standard values for the silicon standard atomic weight $W_A=28.0855(3)$ g mol$^{-1}$ and the molar volume $V_m=(12.058\,836\,9\pm 0.000\,001\,4)\times 10^{-6}$ m$^3$ mol$^{-1}$ [22]. Note that the density $\rho$ was used twice during the calculations of the mass attenuation coefficients $[\mu/\rho]$: to extract the local thickness from the local column thickness $t_{local}=(\rho t_{local})/\rho=(M/A)/\rho$ and to derive the final mass attenuation coefficients $[\mu/\rho]=\ln(I_0/I)/(\rho t)$. Our procedure for mapping the relative x-ray thickness profiles and derives the local (integrated) column density $\rho t_{local}$ from the accurately determined average value $\rho t_{ave}=M/A$. Therefore, since $\rho$ is not used except as (integrated) $\rho t_{local}$ in the derivation of the mass attenuation coefficient, uncertainty in the density $\rho$ does not affect the final

result for the mass attenuation coefficient and only affects the deduced thicknesses using the linear attenuation coefficient.

The average thickness of the thickest crystal obtained was $t_{av}=(3.8992\pm0.0018)$ mm (or $\pm0.048\%$ precision).

#### *2. Micrometer measurements*

The variation in the thickness of the wafer was measured using a micrometer with a 5 mm diameter contact region at 25 points equally spaced over the $15\times15$ mm$^2$ surface of the wafer. The accuracy and reproducibility of each micrometer measurement was 0.5 $\mu$m, and showed that the variation in local thickness measured with the micrometer was about 0.23%. The percent variation in thickness generally increases dramatically for thinner samples. The average thickness of the entire 4-mm-thick specimen was

$$t_{micro1,av}=(3.9091\pm0.0001)\ \text{mm}\ (\pm0.0026\%). \quad (1)$$

The average thickness obtained from the mean of local micrometer readings in Eq. (1) is higher than that obtained from measuring the mass and surface area, by 11 $\mu$m or 0.28%. This is expected due to the variation in the thickness of the crystal as found in the micrometer measurements and the fact that the micrometer always rests on the thickest part within its footprint. Profiles of the microstructures on the crystal surface obtained with a tencor instruments profilometer confirmed this level of surface structures, of a few microns. This effect becomes relatively more significant for thinner wafers and must be accounted for by applying the thickness transfer procedure discussed in Refs. [20,23].

#### *3. X-ray two-dimensional mapping*

In addition, we scanned a 20 keV, $1\times1$ mm$^2$ x-ray beam over the central region of the wafer in $0.4\times0.8$ mm$^2$ steps over an $8\times8$ mm$^2$ square area to obtain a precise measurement of the variation in the local column thickness of the wafer. This measurement is directly related to the attenuation measurements themselves, and allows for any spatial nonuniformity of the local thickness of the wafer or (close to negligible) divergence of the beam, covering exactly the same region as the attenuation measurement itself. It therefore yields a high statistical precision of the local average thickness directly relevant to the experiment and using the same x-ray beam.

We note that the variation of the local thickness of the wafer $t_{local}$ is proportional to the variation of the log of the intensity ratios:

$$t_{local}\propto[\mu/\rho]\rho\times t_{local} = \ln\left(\frac{I_{down,0}}{I_{up,0}}\Big/\frac{I_{down}}{I_{up}}\right), \quad (2)$$

where $I_{up}$ and $I_{down}$ are the upstream and downstream ion chamber readings when one of the specimen was inserted into the beam (corrected for the ion chamber readings when the beam is off), and $I_{up,0}$ and $I_{down,0}$ are the corresponding direct-beam intensities.

The variation in attenuation ($\mu t$) obtained using x-ray two-dimensional mapping agrees with the 0.2%–0.3% variations in local thickness observed using micrometry, the profilometry, and their discrepancies compared to the average thickness obtained from the weighing of a wafer of known area.

#### *4. Combining the results of the above thickness measurements*

The information from the absolute micrometer measurements and the highly precise relative x-ray measurements was combined by means of the procedure discussed in Ref. [20] to yield the thickness over the actual $1\times1$ mm$^2$ area through which the beam passed during the attenuation experiment. The positions of the micrometer footprints were fitted using a least-square-fitting computer program to match the central $8\times8$ mm$^2$ area whose thickness variation was measured both with the micrometer and the x-ray beam. A more detailed description of this program has been given in Ref. [21]. The detailed map of the absolute variation in the local thickness $t_{X\text{-}ray}$ has the average value $t_{X\text{-}ray,av}=3.9016$ mm with a corresponding uncertainty of 0.022%.

The average thickness of the area over which the x-ray scan was taken can also be determined by averaging all the micrometer measurements taken over the overlap area with weighting coefficients: 1 for points that are not on the area boundary, 0.5 for points that are on the boundary but not at a corner, and 0.25 for the four points at the corners,

$$t_{micro2,av}=(3.9106\pm0.00025)\ \text{mm}\ (\pm0.006\%). \quad (3)$$

Combining the results from Eqs. (1)–(3), the local thickness of the sample can be determined by subtracting the correction for the surface structure and the variation in the local thickness from the calibrated local thickness (obtained from the calibration of the x-ray scan). The resulting local thickness of the $1\times1$ mm$^2$ region used in our experiment was

$$t_{local}=(3.9089\pm0.0022)\ \text{mm}\ (\pm\ 0.06\%). \quad (4)$$

### B. Determination of the thicknesses of the thinner wafers

The direct thickness measurements described above were carried out for the thickest 4-mm wafer, where the relative error in the measurement was smallest. The next thickest wafer was related to the thickest one by a comparison of the attenuation of the two wafers at the same x-ray energy. Similarly, the thinner wafers were compared to the thicker ones using a lower-energy x-ray beam. The same size x-ray beam was used in all relative measurements. When changing wafers, care was taken to retain at least one wafer in the same mounting as in the previous measurement. Hence, ultimately all thickness measurements were related to the thickest wafer whose absolute thickness was determined by the combination of techniques described above.

TABLE I. Measured mass attenuation coefficients $[\mu/\rho]$ and the imaginary part of the atomic form factor of silicon $f''$ as a function of energy $E$ ($E^*$ = directly measured energy), with estimated uncertainties: $\sigma_E$, absolute uncertainty in calibrated energy (one standard deviation); $\sigma_{\mu,ste}$, percentage precision of repeated measurements (one standard error); $\sigma_t$, percentage accuracy in sample thickness determination; $\sigma_{[\mu/\rho]}$: total percentage accuracy in measured $[\mu/\rho]$; $f''_{Ch}$, after subtraction of scattering contribution following Chantler [16]. $f''_{XCOM}$: after subtraction of scattering contribution following XCOM [18,24]; $\sigma_{f''}$, absolute uncertainty in $f''$. Numbers in brackets [ ] indicate powers of ten.

| $E$ (keV) | $\sigma_E$ (eV) | $[\mu/\rho]$ ($cm^2/g$) | $\sigma_{\mu,ste}$ (%) | $\sigma_t$ (%) | $\sigma_{[\mu/\rho]}$ (%) | $f''_{Ch}$ ($e$/atom) | $f''_{XCOM}$ ($e$/atom) | $\sigma_{f''}$ ($e$/atom) |
|---|---|---|---|---|---|---|---|---|
| 5.0146* | 1.52 | 244.247 | 0.321 | 0.139 | 0.350 | 8.170[E−01] | 8.170[E−01] | 2.856[E−03] |
| 5.1133 | 1.31 | 231.275 | 0.292 | 0.139 | 0.323 | 7.888[E−01] | 7.888[E−01] | 2.551[E−03] |
| 5.2126 | 1.29 | 218.775 | 0.327 | 0.139 | 0.356 | 7.606[E−01] | 7.606[E−01] | 2.705[E−03] |
| 5.3120 | 1.30 | 207.209 | 0.313 | 0.139 | 0.343 | 7.341[E−01] | 7.341[E−01] | 2.516[E−03] |
| 5.4116 | 1.30 | 197.271 | 0.307 | 0.139 | 0.337 | 7.119[E−01] | 7.119[E−01] | 2.399[E−03] |
| 5.5113 | 1.28 | 186.718 | 0.316 | 0.139 | 0.345 | 6.862[E−01] | 6.862[E−01] | 2.369[E−03] |
| 5.6115 | 1.24 | 177.229 | 0.319 | 0.139 | 0.348 | 6.632[E−01] | 6.631[E−01] | 2.305[E−03] |
| 5.7111 | 1.19 | 168.356 | 0.145 | 0.139 | 0.200 | 6.411[E−01] | 6.411[E−01] | 1.285[E−03] |
| 5.8111 | 1.13 | 159.869 | 0.138 | 0.139 | 0.195 | 6.194[E−01] | 6.194[E−01] | 1.210[E−03] |
| 6.0110* | 1.02 | 145.860 | 0.164 | 0.139 | 0.215 | 5.845[E−01] | 5.845[E−01] | 1.255[E−03] |
| 6.1110 | 0.98 | 139.672 | 0.084 | 0.139 | 0.162 | 5.690[E−01] | 5.689[E−01] | 9.236[E−04] |
| 6.2110 | 0.94 | 133.244 | 0.044 | 0.139 | 0.145 | 5.516[E−01] | 5.516[E−01] | 8.023[E−04] |
| 6.3110 | 0.90 | 127.224 | 0.036 | 0.139 | 0.143 | 5.351[E−01] | 5.351[E−01] | 7.664[E−04] |
| 6.4110 | 0.88 | 121.450 | 0.030 | 0.139 | 0.142 | 5.189[E−01] | 5.189[E−01] | 7.366[E−04] |
| 6.5110 | 0.87 | 116.141 | 0.043 | 0.139 | 0.145 | 5.039[E−01] | 5.039[E−01] | 7.312[E−04] |
| 6.6110 | 0.86 | 111.117 | 0.012 | 0.139 | 0.139 | 4.895[E−01] | 4.895[E−01] | 6.812[E−04] |
| 6.7110 | 0.88 | 106.360 | 0.030 | 0.139 | 0.142 | 4.756[E−01] | 4.755[E−01] | 6.748[E−04] |
| 6.8110 | 0.90 | 101.882 | 0.017 | 0.139 | 0.140 | 4.623[E−01] | 4.623[E−01] | 6.457[E−04] |
| 6.9110 | 0.93 | 97.644 | 0.029 | 0.139 | 0.142 | 4.495[E−01] | 4.495[E−01] | 6.372[E−04] |
| 7.0110* | 0.97 | 93.625 | 0.021 | 0.139 | 0.140 | 4.372[E−01] | 4.372[E−01] | 6.131[E−04] |
| 7.0110 | 0.97 | 93.578 | 0.020 | 0.139 | 0.140 | 4.370[E−01] | 4.370[E−01] | 6.123[E−04] |
| 7.1117 | 0.87 | 89.788 | 0.057 | 0.139 | 0.150 | 4.253[E−01] | 4.253[E−01] | 6.384[E−04] |
| 7.2061 | 0.80 | 86.627 | 0.009 | 0.139 | 0.139 | 4.157[E−01] | 4.157[E−01] | 5.777[E−04] |
| 7.3131 | 0.76 | 83.143 | 0.144 | 0.139 | 0.200 | 4.049[E−01] | 4.049[E−01] | 8.099[E−04] |
| 7.4138* | 0.78 | 79.884 | 0.022 | 0.139 | 0.140 | 3.943[E−01] | 3.943[E−01] | 5.536[E−04] |
| 7.5134 | 0.74 | 76.856 | 0.121 | 0.139 | 0.184 | 3.844[E−01] | 3.844[E−01] | 7.071[E−04] |
| 7.6130* | 0.35 | 73.826 | 0.080 | 0.139 | 0.160 | 3.741[E−01] | 3.741[E−01] | 5.980[E−04] |
| 7.6130 | 0.35 | 73.827 | 0.052 | 0.139 | 0.148 | 3.741[E−01] | 3.741[E−01] | 5.545[E−04] |
| 7.7130 | 0.27 | 71.168 | 0.167 | 0.139 | 0.217 | 3.654[E−01] | 3.653[E−01] | 7.944[E−04] |
| 7.8135 | 0.22 | 68.509 | 0.021 | 0.139 | 0.140 | 3.563[E−01] | 3.562[E−01] | 4.997[E−04] |
| 8.0134* | 0.26 | 63.894 | 0.037 | 0.139 | 0.143 | 3.407[E−01] | 3.406[E−01] | 4.885[E−04] |
| 8.0135 | 0.26 | 63.856 | 0.090 | 0.115 | 0.146 | 3.405[E−01] | 3.404[E−01] | 4.969[E−04] |
| 8.1133 | 0.25 | 61.572 | 0.049 | 0.115 | 0.125 | 3.323[E−01] | 3.323[E−01] | 4.150[E−04] |
| 8.2136 | 0.26 | 59.296 | 0.039 | 0.115 | 0.121 | 3.240[E−01] | 3.239[E−01] | 3.929[E−04] |
| 8.3138 | 0.29 | 57.227 | 0.014 | 0.115 | 0.116 | 3.164[E−01] | 3.164[E−01] | 3.664[E−04] |
| 8.4144 | 0.33 | 55.237 | 0.041 | 0.115 | 0.122 | 3.091[E−01] | 3.090[E−01] | 3.770[E−04] |
| 8.5143 | 0.39 | 53.349 | 0.033 | 0.115 | 0.120 | 3.020[E−01] | 3.020[E−01] | 3.610[E−04] |
| 8.6143 | 0.45 | 51.545 | 0.057 | 0.115 | 0.128 | 2.952[E−01] | 2.951[E−01] | 3.789[E−04] |
| 8.7143 | 0.52 | 49.836 | 0.016 | 0.115 | 0.116 | 2.887[E−01] | 2.886[E−01] | 3.349[E−04] |
| 8.8149 | 0.59 | 48.176 | 0.055 | 0.115 | 0.127 | 2.822[E−01] | 2.822[E−01] | 3.593[E−04] |
| 8.9150 | 0.66 | 46.607 | 0.014 | 0.115 | 0.116 | 2.761[E−01] | 2.760[E−01] | 3.197[E−04] |
| 9.0155* | 0.74 | 45.184 | 0.147 | 0.115 | 0.186 | 2.707[E−01] | 2.706[E−01] | 5.040[E−04] |
| 9.1159 | 0.66 | 43.697 | 0.076 | 0.115 | 0.138 | 2.646[E−01] | 2.646[E−01] | 3.654[E−04] |
| 9.2159 | 0.59 | 42.342 | 0.028 | 0.115 | 0.118 | 2.592[E−01] | 2.591[E−01] | 3.069[E−04] |
| 9.3158 | 0.53 | 41.081 | 0.072 | 0.115 | 0.135 | 2.541[E−01] | 2.541[E−01] | 3.443[E−04] |
| 9.4156 | 0.46 | 39.737 | 0.081 | 0.115 | 0.141 | 2.484[E−01] | 2.484[E−01] | 3.498[E−04] |
| 9.5159 | 0.40 | 38.486 | 0.087 | 0.115 | 0.144 | 2.431[E−01] | 2.431[E−01] | 3.509[E−04] |
| 9.6158 | 0.36 | 37.306 | 0.091 | 0.115 | 0.147 | 2.381[E−01] | 2.380[E−01] | 3.497[E−04] |
| 9.7164 | 0.32 | 36.273 | 0.120 | 0.115 | 0.166 | 2.339[E−01] | 2.338[E−01] | 3.884[E−04] |

TABLE I. (*Continued*).

| $E$ (keV) | $\sigma_E$ (eV) | $[\mu/\rho]$ ($cm^2/g$) | $\sigma_{\mu,ste}$ (%) | $\sigma_t$ (%) | $\sigma_{[\mu/\rho]}$ (%) | $f''_{Ch}$ ($e$/atom) | $f''_{XCOM}$ ($e$/atom) | $\sigma_{f''}$ ($e$/atom) |
|---|---|---|---|---|---|---|---|---|
| 9.8164 | 0.30 | 35.151 | 0.074 | 0.115 | 0.137 | 2.289[E−01] | 2.289[E−01] | 3.128[E−04] |
| 9.9171 | 0.31 | 34.112 | 0.125 | 0.115 | 0.170 | 2.244[E−01] | 2.243[E−01] | 3.816[E−04] |
| 10.0168 | 0.33 | 33.104 | 0.027 | 0.115 | 0.118 | 2.199[E−01] | 2.199[E−01] | 2.598[E−04] |
| 10.0172* | 0.33 | 33.074 | 0.184 | 0.115 | 0.217 | 2.197[E−01] | 2.197[E−01] | 4.767[E−04] |
| 10.0172 | 0.33 | 33.082 | 0.184 | 0.115 | 0.217 | 2.198[E−01] | 2.197[E−01] | 4.773[E−04] |
| 10.1168 | 0.31 | 32.129 | 0.033 | 0.115 | 0.120 | 2.155[E−01] | 2.155[E−01] | 2.577[E−04] |
| 10.2176 | 0.29 | 31.185 | 0.122 | 0.115 | 0.168 | 2.112[E−01] | 2.112[E−01] | 3.549[E−04] |
| 10.3176 | 0.30 | 30.300 | 0.067 | 0.115 | 0.133 | 2.072[E−01] | 2.071[E−01] | 2.755[E−04] |
| 10.4179 | 0.32 | 29.437 | 0.148 | 0.115 | 0.187 | 2.032[E−01] | 2.032[E−01] | 3.804[E−04] |
| 10.5181 | 0.35 | 28.615 | 0.045 | 0.115 | 0.123 | 1.994[E−01] | 1.993[E−01] | 2.462[E−04] |
| 10.6185 | 0.39 | 27.910 | 0.012 | 0.115 | 0.116 | 1.963[E−01] | 1.962[E−01] | 2.269[E−04] |
| 10.7191 | 0.44 | 27.164 | 0.025 | 0.115 | 0.118 | 1.928[E−01] | 1.928[E−01] | 2.271[E−04] |
| 10.8203 | 0.49 | 26.325 | 0.179 | 0.115 | 0.213 | 1.886[E−01] | 1.885[E−01] | 4.014[E−04] |
| 10.9203 | 0.55 | 25.690 | 0.033 | 0.115 | 0.120 | 1.857[E−01] | 1.856[E−01] | 2.220[E−04] |
| 11.0202* | 0.61 | 24.972 | 0.138 | 0.115 | 0.179 | 1.821[E−01] | 1.821[E−01] | 3.266[E−04] |
| 11.1197 | 0.56 | 24.326 | 0.114 | 0.115 | 0.162 | 1.790[E−01] | 1.789[E−01] | 2.901[E−04] |
| 11.2199 | 0.52 | 23.667 | 0.014 | 0.115 | 0.116 | 1.757[E−01] | 1.756[E−01] | 2.035[E−04] |
| 11.3198 | 0.50 | 23.018 | 0.205 | 0.115 | 0.235 | 1.723[E−01] | 1.723[E−01] | 4.047[E−04] |
| 11.4203 | 0.50 | 22.428 | 0.088 | 0.115 | 0.145 | 1.693[E−01] | 1.693[E−01] | 2.456[E−04] |
| 11.5200 | 0.52 | 21.958 | 0.165 | 0.115 | 0.201 | 1.672[E−01] | 1.671[E−01] | 3.358[E−04] |
| 11.6203 | 0.56 | 21.364 | 0.021 | 0.115 | 0.117 | 1.641[E−01] | 1.640[E−01] | 1.918[E−04] |
| 11.7199 | 0.61 | 20.859 | 0.135 | 0.115 | 0.177 | 1.615[E−01] | 1.614[E−01] | 2.858[E−04] |
| 11.8202 | 0.68 | 20.260 | 0.017 | 0.115 | 0.116 | 1.582[E−01] | 1.581[E−01] | 1.838[E−04] |
| 11.9211 | 0.76 | 19.823 | 0.068 | 0.115 | 0.134 | 1.561[E−01] | 1.560[E−01] | 2.085[E−04] |
| 12.0209* | 0.84 | 19.337 | 0.021 | 0.115 | 0.117 | 1.535[E−01] | 1.534[E−01] | 1.793[E−04] |
| 12.0209 | 0.84 | 19.336 | 0.019 | 0.115 | 0.117 | 1.535[E−01] | 1.534[E−01] | 1.789[E−04] |
| 12.1711 | 0.76 | 18.617 | 0.006 | 0.115 | 0.115 | 1.495[E−01] | 1.495[E−01] | 1.721[E−04] |
| 12.3210 | 0.68 | 17.924 | 0.055 | 0.115 | 0.127 | 1.457[E−01] | 1.456[E−01] | 1.854[E−04] |
| 12.4703 | 0.60 | 17.290 | 0.071 | 0.115 | 0.135 | 1.422[E−01] | 1.421[E−01] | 1.919[E−04] |
| 12.6208 | 0.53 | 16.669 | 0.116 | 0.115 | 0.164 | 1.386[E−01] | 1.386[E−01] | 2.269[E−04] |
| 12.7706 | 0.48 | 16.092 | 0.043 | 0.115 | 0.123 | 1.354[E−01] | 1.353[E−01] | 1.663[E−04] |
| 12.9206 | 0.43 | 15.521 | 0.100 | 0.115 | 0.152 | 1.320[E−01] | 1.320[E−01] | 2.009[E−04] |
| 13.0706 | 0.40 | 15.018 | 0.079 | 0.115 | 0.139 | 1.292[E−01] | 1.291[E−01] | 1.801[E−04] |
| 13.2208 | 0.40 | 14.533 | 0.078 | 0.115 | 0.139 | 1.264[E−01] | 1.263[E−01] | 1.756[E−04] |
| 13.3715 | 0.42 | 14.056 | 0.152 | 0.115 | 0.191 | 1.236[E−01] | 1.235[E−01] | 2.357[E−04] |
| 13.5215* | 0.45 | 13.559 | 0.109 | 0.115 | 0.159 | 1.205[E−01] | 1.204[E−01] | 1.911[E−04] |
| 13.6713 | 0.41 | 13.137 | 0.082 | 0.115 | 0.141 | 1.180[E−01] | 1.179[E−01] | 1.666[E−04] |
| 13.8220 | 0.39 | 12.755 | 0.038 | 0.115 | 0.121 | 1.157[E−01] | 1.157[E−01] | 1.402[E−04] |
| 13.9721 | 0.39 | 12.314 | 0.104 | 0.115 | 0.155 | 1.129[E−01] | 1.128[E−01] | 1.748[E−04] |
| 14.1224 | 0.41 | 11.983 | 0.153 | 0.115 | 0.192 | 1.110[E−01] | 1.109[E−01] | 2.128[E−04] |
| 14.2723 | 0.45 | 11.551 | 0.137 | 0.115 | 0.179 | 1.081[E−01] | 1.080[E−01] | 1.931[E−04] |
| 14.4228 | 0.50 | 11.222 | 0.240 | 0.115 | 0.266 | 1.060[E−01] | 1.059[E−01] | 2.819[E−04] |
| 14.5744 | 0.56 | 10.903 | 0.085 | 0.115 | 0.143 | 1.040[E−01] | 1.040[E−01] | 1.490[E−04] |
| 14.7240 | 0.63 | 10.544 | 0.194 | 0.115 | 0.225 | 1.016[E−01] | 1.015[E−01] | 2.290[E−04] |
| 14.8759 | 0.70 | 10.254 | 0.346 | 0.115 | 0.365 | 9.976[E−02] | 9.967[E−02] | 3.641[E−04] |
| 14.8722 | 0.70 | 10.173 | 0.174 | 0.115 | 0.209 | 9.893[E−02] | 9.884[E−02] | 2.064[E−04] |
| 15.0231* | 0.78 | 9.969 | 0.038 | 0.115 | 0.121 | 9.789[E−02] | 9.781[E−02] | 1.186[E−04] |
| 15.2264 | 0.65 | 9.553 | 0.215 | 0.115 | 0.243 | 9.499[E−02] | 9.491[E−02] | 2.312[E−04] |
| 15.4259 | 0.55 | 9.195 | 0.141 | 0.115 | 0.182 | 9.255[E−02] | 9.247[E−02] | 1.683[E−04] |
| 15.6253 | 0.48 | 8.857 | 0.112 | 0.115 | 0.161 | 9.023[E−02] | 9.015[E−02] | 1.449[E−04] |
| 15.8256 | 0.46 | 8.522 | 0.099 | 0.115 | 0.152 | 8.785[E−02] | 8.777[E−02] | 1.332[E−04] |
| 16.0255 | 0.49 | 8.214 | 0.121 | 0.115 | 0.167 | 8.567[E−02] | 8.559[E−02] | 1.433[E−04] |

TABLE I. (*Continued*).

| $E$ (keV) | $\sigma_E$ (eV) | $[\mu/\rho]$ ($cm^2/g$) | $\sigma_{\mu,ste}$ (%) | $\sigma_t$ (%) | $\sigma_{[\mu/\rho]}$ (%) | $f''_{Ch}$ ($e$/atom) | $f''_{XCOM}$ ($e$/atom) | $\sigma_{f''}$ ($e$/atom) |
|---|---|---|---|---|---|---|---|---|
| 16.2252* | 0.56 | 7.921 | 0.053 | 0.115 | 0.126 | 8.356[$E-02$] | 8.348[$E-02$] | 1.057[$E-04$] |
| 16.2257 | 0.56 | 7.913 | 0.055 | 0.115 | 0.127 | 8.348[$E-02$] | 8.341[$E-02$] | 1.064[$E-04$] |
| 16.4246 | 0.50 | 7.647 | 0.037 | 0.115 | 0.121 | 8.159[$E-02$] | 8.152[$E-02$] | 9.850[$E-05$] |
| 16.6252 | 0.46 | 7.390 | 0.096 | 0.115 | 0.150 | 7.974[$E-02$] | 7.966[$E-02$] | 1.196[$E-04$] |
| 16.8272 | 0.47 | 7.116 | 0.138 | 0.115 | 0.180 | 7.763[$E-02$] | 7.755[$E-02$] | 1.395[$E-04$] |
| 17.0274 | 0.51 | 6.865 | 0.176 | 0.115 | 0.210 | 7.571[$E-02$] | 7.563[$E-02$] | 1.593[$E-04$] |
| 17.2278 | 0.59 | 6.633 | 0.049 | 0.115 | 0.125 | 7.393[$E-02$] | 7.385[$E-02$] | 9.226[$E-05$] |
| 17.4276 | 0.68 | 6.405 | 0.051 | 0.115 | 0.126 | 7.214[$E-02$] | 7.206[$E-02$] | 9.076[$E-05$] |
| 17.6276 | 0.79 | 6.174 | 0.125 | 0.115 | 0.170 | 7.025[$E-02$] | 7.017[$E-02$] | 1.191[$E-04$] |
| 17.6284* | 0.79 | 6.165 | 0.067 | 0.060 | 0.090 | 7.015[$E-02$] | 7.007[$E-02$] | 6.336[$E-05$] |
| 17.8270 | 0.65 | 5.974 | 0.132 | 0.060 | 0.145 | 6.867[$E-02$] | 6.859[$E-02$] | 9.975[$E-05$] |
| 18.0274 | 0.54 | 5.764 | 0.046 | 0.060 | 0.076 | 6.692[$E-02$] | 6.683[$E-02$] | 5.074[$E-05$] |
| 18.2259 | 0.50 | 5.583 | 0.438 | 0.060 | 0.442 | 6.546[$E-02$] | 6.538[$E-02$] | 2.893[$E-04$] |
| 18.4269 | 0.55 | 5.427 | 0.146 | 0.060 | 0.158 | 6.427[$E-02$] | 6.418[$E-02$] | 1.014[$E-04$] |
| 18.6266 | 0.65 | 5.249 | 0.094 | 0.060 | 0.112 | 6.275[$E-02$] | 6.266[$E-02$] | 7.029[$E-05$] |
| 18.6272* | 0.65 | 5.229 | 0.105 | 0.060 | 0.121 | 6.250[$E-02$] | 6.241[$E-02$] | 7.576[$E-05$] |
| 18.8253 | 0.57 | 5.079 | 0.084 | 0.060 | 0.104 | 6.129[$E-02$] | 6.120[$E-02$] | 6.358[$E-05$] |
| 19.0264 | 0.50 | 4.939 | 0.344 | 0.060 | 0.350 | 6.017[$E-02$] | 6.008[$E-02$] | 2.104[$E-04$] |
| 19.2255 | 0.46 | 4.772 | 0.058 | 0.060 | 0.083 | 5.865[$E-02$] | 5.856[$E-02$] | 4.889[$E-05$] |
| 19.4241 | 0.46 | 4.629 | 0.022 | 0.060 | 0.064 | 5.741[$E-02$] | 5.732[$E-02$] | 3.679[$E-05$] |
| 19.6246 | 0.49 | 4.496 | 0.119 | 0.060 | 0.133 | 5.627[$E-02$] | 5.618[$E-02$] | 7.490[$E-05$] |
| 19.8238 | 0.55 | 4.354 | 0.109 | 0.060 | 0.125 | 5.497[$E-02$] | 5.488[$E-02$] | 6.857[$E-05$] |
| 20.0281* | 0.63 | 4.228 | 0.084 | 0.060 | 0.103 | 5.385[$E-02$] | 5.376[$E-02$] | 5.573[$E-05$] |

This transfer procedure made small contributions to the final uncertainties in the determination of the local thicknesses of the thinner specimens. These are summarized in Table II.

## IV. X-RAY ENERGY CALIBRATION

The attenuation measurements were carried out at more than 120 energies between 5 keV and 20 keV. The energies of the incident beam were measured directly at 16 points (marked by asterisks in Table I) within this energy range from the powder diffraction patterns of two standards: Si640b ($a_0 = 5.430\,940(11)$ Å [4]) and $LaB_6$ [$a_0 = 4.15695(6)$ Å—NIST standard] in the ANBF diffractometer chamber (BigDiff) [25–27]. Details of the BigDiff apparatus and the interpretation of the powder patterns have been discussed elsewhere [20]. The directly measured energies were used to calibrate the monochromator encoder settings from which the intermediate energies were obtained.

The directly measured energies differed from the nominal monochromator energies by 10 eV–30 eV. The uncertainties of the direct energy measurements ranged from 0.2 eV to 1.6 eV. The direct energy measurements using the silicon standard were in agreement with those obtained with $LaB_6$ within the corresponding measurement uncertainties $\sigma$ of each standard, except at 9 keV and 17.6 keV where the discrepancies were $1.3\sigma$ and $1.6\sigma$, respectively. The final energies used in the calibration were a weighted average of the energies obtained with the two standards.

These directly measured weighted average energies $E$ are marked with an asterisk in Table I, which also lists the interpolated calibrated energies. The correspoding estimated errors $\sigma_E$ are also listed and include the effect of a very slow drift of the monochromator encoder axis, which was found to occur after the axis was commanded to stop. This only affected measurements for which the energy was interpolated. The magnitude of this effect was 0.2 eV at and below 7.6 keV and 1.7 eV at 20 keV, with the uncertainty of the correction rising from $\pm 0.1$ eV to $\pm 0.35$ eV due to the energy drift between sets of measurements at the same nominal energy.

## V. OPTIMIZATION OF SYSTEM STATISTICS

The counting methods employed in our measurements have been discussed in Refs. [20,28,29]. We measured and modeled various factors contributing to the final counting statistics including beam decay, beam fluctuations, fluctuations in the detector absorption, and in air absorption. We showed that a simple Gaussian model does not adequately describe the system statistics and that the correlation function between different time-varying components affects significantly the final counting statistics. We found that in order to optimize the system statistics, components that result in negative correlations between the readings of the two ion

TABLE II. Summary of the main sources of uncertainties of the measured mass attenuation coefficient $[\mu/\rho]$, the photoelectric absorption coefficient $[\mu/\rho]_{pe}$, and $f''$ of silicon.

| Source of uncertainty | Contribution 5−5.6 keV | Contribution 5.6−20 keV | Notes ±1 standard error |
|---|---|---|---|
| Major contributions to precision: | | | |
| Harmonic contamination | ≈0.3% | | |
| Bragg diffraction | | <0.44% | Maximal at 18.226 keV |
| Monochromator hysteresis | <0.07% | | $\sigma_E$<1.3 eV at 5 keV−6 keV |
| Energy calibration elsewhere | 0.01% | 0.01% | $\sigma_E/E=\pm 0.004\%$ |
| System statistics | 0.02% | 0.02% | Reproducibility without sample |
| Major contributions to accuracy: | | | |
| Experimental precision | 0.3% | 0.02%−0.44% | Including all above contributions |
| Sample thickness | 0.139% | 0.06%−0.139% | Thickness calibration and transfer |
| Minor contributions: | | | |
| Energy drift | | 0.00%−0.008% | $\sigma_E/E=\pm 0.0026\%$ at 7.6 keV<br>$\sigma_E/E=\pm 0.001\,75\%$ at 20 keV |
| Additional contributions: | | | |
| For $[\mu/\rho]_{pe}$ and Im(f): | | | |
| Compton, TDS | Minor | 0.05% | Variation in theory |
| Total final accuracy | 0.323%−0.350% | 0.064%−0.266% | Outliers 0.365% (at 14.879 keV)<br>And 0.442% (at 18.226 keV)<br>Due to Bragg diffraction |

chambers should be minimized and components that result in positive correlations between these readings should be maximized.

Figure 2 shows the correlation coefficients $R$ between the two readings of the upstream and downstream ion chambers during the measurements. The ion chamber readings are strongly positively correlated for most measurements, confirming that the detection system was optimized as discussed in Refs. [20,28,29]. For measurements using thick specimens, the readings of the two ion chambers were uncorrelated resulting in a few negative values of $R$ in Fig. 2. This had a small effect on counting statistics but was crucial for investigations of dominant sources of systematic errors including harmonic component determination and dark current detector offsets.

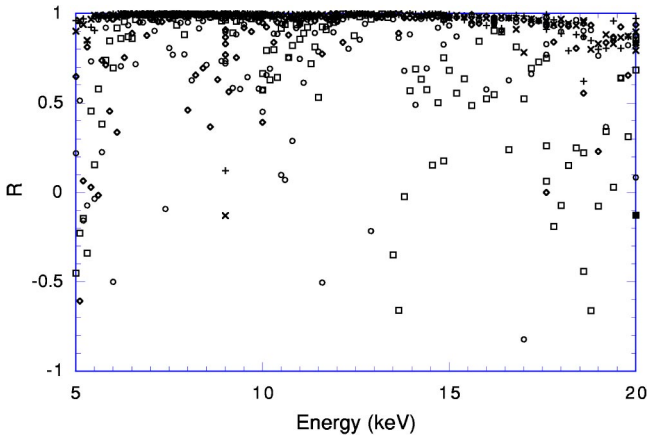


FIG. 2. Correlation coefficients $R$ between the readings of the upstream and downstream ion chambers: specimen 1 (hollow circle); blank 1 (hollow square); specimen 2 (hollow diamond); blank 2 (black square); specimen 3 (black diamond). The fact that most of the measured values of $R$ were close to one demonstrates that the counting statistics were optimized. Negative $R$ values are discussed in the text.

The reproducibility of the measurements was tested by comparing the intensity ratios of two series of direct-beam measurements over the entire energy range. Fluctuations of $\pm 0.02\%$ were observed (Fig. 3). This level of reproducibility allows accurate investigation of other sources of systematic errors.

## VI. CORRECTION FOR THE HARMONIC CONTRIBUTION AND LINEARITY OF DETECTOR RESPONSE

It is well known that a crystal monochromator selects from the incident x-ray spectrum a series of harmonics all of which satisfy the Bragg condition for a given setting of the monochromator. In the case of a [111] silicon monochromator the second-order harmonic is quasiforbidden, its intensity being certainly negligible compared to the fundamental, very intense (111) reflection. A contribution of the third-order harmonic is possible, while higher orders were beyond the cutoff energy of the synchrotron spectrum.

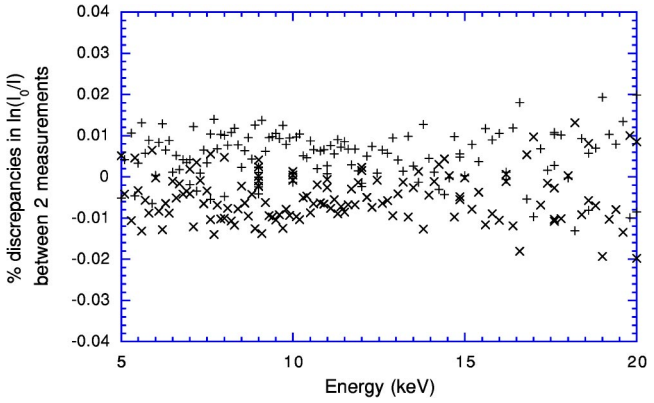


FIG. 3. Reproducibility of direct-beam measurements as a function of energy, × first set of measurements, + second set of measurements. We plot the percent discrepancy of the ratio of the detector count divided by the monitor count, compared to the average of the two datasets. The observed 0.02% reproducibility, a result of the optimization of the counting system, makes it possible to investigate sources of systematic errors observable above this magnitude.

In our experiment, the third-harmonic component in the x-ray beam was minimized both by the incident flux at the higher energy, being lower, and by detuning the second reflecting plane of the double-reflection silicon monochromator. Nevertheless, much to our surprise, we found below 5.6 keV strong evidence of the presence of the third-order harmonic contamination in the incident x-ray beam.

Figure 4 shows a comparison between the measured mass attenuation coefficients $[\mu/\rho]$ for wafers of three thicknesses and that predicted by theory [16]. Above 5.6 keV, the three measurements are consistent to well within 1% and confirm the general trend predicted by theory. This indicates that the measurements were free from harmonic contamination in this higher-energy range (the same conclusion was found in our early work of copper in the energy ranging from 8.85 keV to 20 keV [20]). Below 5.6 keV, the measured $[\mu/\rho]$ decreases systematically with increasing thickness. This is

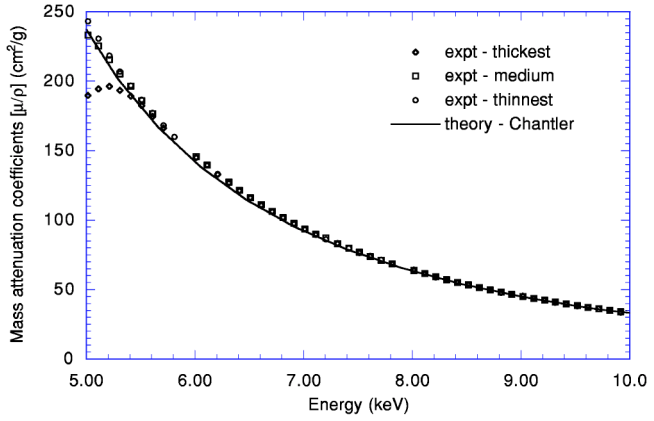


FIG. 4. Results of the measurements of the mass attenuation coefficient of silicon. On the scale of this graph the measurements obtained with the three wafer thicknesses overlap. The signature of the effect of the harmonic content in the incident beam is seen below 5.6 keV as discussed in the text.

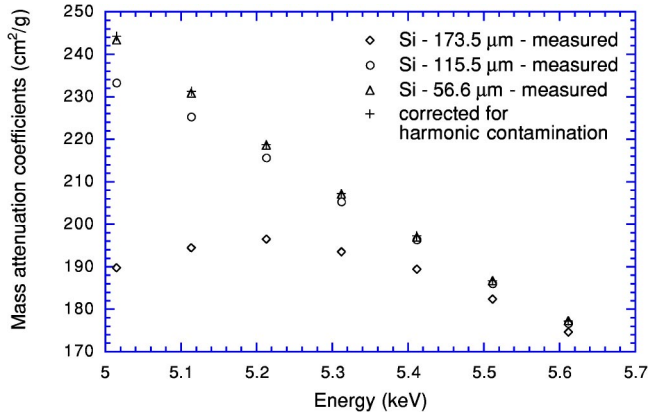


FIG. 5. Effect of third-order harmonic contamination on the mass attenuation coefficients $[\mu/\rho]$ with a Si(111) monochromator and three silicon wafers. Triangles, squares, and diamonds represent the measured mass attenuation coefficients corresponding to the thinnest (56.3 $\mu$m), medium (115.4 $\mu$m) and thickest (171.9 $\mu$m) silicon wafers, respectively. Crosses represent the attenuation coefficients corrected for the effect of harmonic contamination.

the effect of harmonic contamination in the beam which occur only in the lower-energy region.

Note that signatures of harmonic contamination and of multiple scattering are almost indistinguishable in previous experimental work, where single isolated energies were investigated. Because of our XERT technique, the signatures are clearly separated and this is why we can reject multiple scattering as a possible cause of the systematic. In the data, the reported systematic discrepancy occurred only in the low-energy region (consistent with the effect of harmonic contamination). If multiple scattering was the cause then the discrepancy would have occurred more strongly in the higher-energy region where contributions from scattering are larger. Complex multiple scattering can also peak near edges but this is also not the signature observed (in fact, we have no edges in the dataset).

Multiple-sample measurements can be used as a sensitive diagnostic technique for the quantitative determination of the fraction of harmonic radiation in a monochromatized x-ray beam. The method can simultaneously provide quantitative information about nonlinear detector response due, for example, to saturation which may occur at high counting rates as discussed elsewhere [30]. By using interpolated values of the measured mass attenuation coefficients between 15 keV and 16.8 keV and allowing the mass attenuation coefficients between 5 keV and 5.6 keV to vary, it is possible to determine the third-harmonic content of the incident x-ray beam.

The technique of using multiple samples of accurately known thickness is quite sensitive and we found that it could reliably establish the level of harmonic contamination at 5.6 keV to within 0.01%. The final accuracy of the technique depends on the accuracy of the thickness measurements, the relative attenuation of the fundamental and harmonic radiation and on counting statistics. Results are plotted in Fig. 5. In our measurements, the correction to the mass attenuation coefficients due to this effect was of the order of 0.3%.

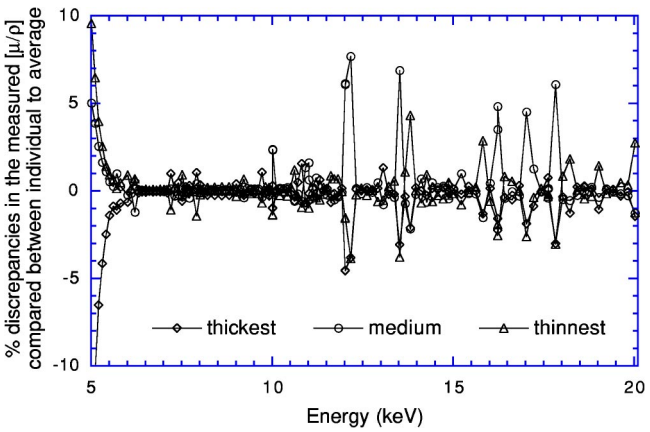


FIG. 6. Percent discrepancy between the measurements of $[\mu/\rho]$ using three samples compared to their average as a function of energy. Below 5.6 keV, the divergence shows the effect of harmonic contamination before applying the correction procedure described in Sec. VI. Above 5.6 keV, the discrepancies are generally less than 0.5%. The spikes in the plot at a series of energies indicate that Bragg diffraction is occurring in that specimen at those energies.

## VII. SCATTERING CONTRIBUTION

The experiment described in the previous sections measures the attenuation of an x-ray beam of given energy after passing through a column of given mass of silicon. The attenuation is due primarily to the photoelectric absorption process. Other processes contribute to the measured attenuation [21], such as Bragg diffraction (by single-crystal silicon), thermal diffuse and Compton scattering, fluorescence resulting from the photoelectric absorption, and any other process which redirects photons from or into the beam direction as the beam passes through the attenuator. Any comparison of the measured attenuation with theory must therefore also take into account these processes either by calculation or by direct measurement of their contributions.

### A. Bragg diffraction

Figure 6 shows the percentage differences in the measured mass attenuation coefficients of the three wafers, compared to the average (zero line). Above 5.6 keV the three measurement results are, in general, consistent within 0.5%. However, we observe some sharp discontinuities (increases between 1% and 8%) in the mass attenuation coefficient measured with one of the wafers compared with the other two consistent measurements.

These discontinuities occur whenever the beam energy and the orientation of a set of planes in the wafer satisfy the Bragg condition. When this occurs, photons from the incident x-ray beam are diffracted and their redirection gives rise to an additional decrease in the attenuated beam. The observed discontinuities in the measured mass attenuation coefficient of one of the wafers depend sharply on the beam energy and the precise orientation of the silicon wafer. This is why only one wafer satisfies the Bragg condition at any one time; although all three wafers are nominally cut parallel to the (111) planes, small misorientations due to their mounting or cutting render the simultaneous satisfaction of the Bragg condition for all three highly unlikely, especially as the silicon crystals are almost perfect and the incident x-ray beam is highly parallel and monochromatized.

Calculation shows that the Bragg condition is satisfied frequently and the effects on the attenuation integrated over the beam divergence are of the correct order of magnitude. Accordingly, in the subset of cases where one of the three measurements appeared more than 0.5% greater than the other two consistent measurements, we rejected the outlying result and used the average mass attenuation value obtained from the two remaining wafers. In all, some 28 values out of the total of 300 points were thus rejected. All results, including those points where one of the three measurements was rejected and those points which were unaffected at the 0.5% level form a smooth curve as shown in Fig. 4.

### B. Thermal diffuse and Compton scattering

Thermal diffuse scattering (TDS) is the result of the dynamic disorder produced in the crystal lattice by the thermal motion of its atoms. In calculating the TDS contribution, we used the approach of Gerward [31], similar to the calculation of Mika *et al.* [13]:

$$\sigma_{TDS}=\frac{1}{2}r_e^2\int_{-1}^{1}(1+\cos^2\Phi)f^2(x,Z)\times(1-e^{-2M(x,Z)})2\pi\delta(\cos\Phi), \tag{5}$$

where $r_e$ is the classical electron radius, $\Phi$ is the angle between the incident and scattered photon, $f=f_0+f'+if''$ is the complex atomic form factor, where $f_0$ is a function of the atomic number $Z$ and the momentum transfer $x=\sin(\Phi/2)/\lambda$, $f',f''$ are energy dependent terms, and $e^{-2M}=e^{-2Bx^2}$ is the Debye-Waller factor with $B=0.468$ Å$^2$ [32].

The scattering factor $f_0$ was determined by linear interpolation of the tabulation given in Ref. [33]. The dispersive scattering factors $f',f''$ were calculated from Ref. [16] or Ref. [18]. The computed TDS contribution to the mass attenuation coefficients ranges from about 0.03% (at 5 keV) to about 1.5% (at 20 keV). The computed Compton scattering contribution ranges from 0.03% (at 5 keV) to 3% (at 20 keV).

Obtaining an accurate photoelectric coefficient involves a single pass through Eq. (6), subtracting these scattering coefficients from the final measured value,

$$[\mu/\rho]_{pe}=[\mu/\rho]_{meas}-[\mu/\rho]_{Compton+TDS}. \tag{6}$$

Therefore, if any result is to be obtained to high accuracy for the experimental value of $f''$, relating directly to atomic (and solid-state) electronic wave functions, then these scattering contributions must be reliable in the higher-energy range. At lower energies, both of these scattering components are relative by small and become an insignificant correction to the total. For the intermediate and higher energies, we have used theoretically calculated values from two major databases. We took the uncertainty in $[\mu/\rho]_{Compton+TDS}$ to

be half the difference between these alternative theoretical calculations. The Compton computations differ by 2% of the Compton magnitude over our energy range and the TDS computations differ by 11% of the TDS magnitude (at 5 keV) and 6% (at 20 keV). Hence, their contribution to the total uncertainty of $[\mu/\rho]_{pe}$ is a mere 0.05%, a rather small contribution to the total uncertainty.

## VIII. RESULTS AND ERROR BUDGET

### A. Results

The energy variation of the mass attenuation coefficients is in agreement with that expected from the isolated atom approximation. The high level of accuracy, the large number and broad distribution of our experimental results over the energy range under investigation allow detailed comparisons between alternative tabulations and are a principal result of this work.

Table I presents our measurements of the mass attenuation coefficient of silicon as a function of energy. The experimental precision and accuracy are one standard deviation estimates based on internal consistency and the quantification of known systematic uncertainties discussed earlier. The imaginary component of the form factor $f''$ is extracted using the calculated Compton and TDS scattering corrections of both Chantler [16] and XCOM [18]. The final uncertainty is dominated at all given energies by the uncertainty of the measured $[\mu/\rho]_{meas}$, $\sigma_{[\mu/\rho]}$, rather than by the model-dependent uncertainty of the scattering coefficients.

The first two columns of Table I list the energies and the corresponding uncertainties. Later columns give the corresponding measured mass attenuation coefficient $[\mu/\rho]$, the experimental precision, the accuracy in the thickness determination, and the total uncertainty of $[\mu/\rho]$, respectively. The last three columns list the imaginary part of the form factor after correction for scattering in accordance with Eq. (6) as discussed in Sec. VII B. Uncertainties in the theoretically calculated scattering components are indicated by the difference between the two model-dependent estimates of $f''$ in the table. This latter uncertainty is clearly insignificant in the lower-energy region, and contributes at most 0.05% as one approaches 20 keV.

Above 5.6 keV the experimental values of $[\mu/\rho]$ are the weighted mean of the measurements obtained with the three thicknesses, excluding those points affected by Bragg diffraction. The final uncertainty in the mass attenuation coefficient $\sigma_{[\mu/\rho]}$ in this range is the root mean square of the contributions from the uncertainty in the thickness calibration $\sigma_t$, and from the consistency of the measurements of using different samples $\sigma_{ste}$:

$$\sigma_{ste}=\sqrt{\frac{\sum_{all}\frac{([\mu/\rho]_{t_i}-\overline{[\mu/\rho]})^2}{\sigma_i^2}}{\sum_{all}1/\sigma_i^2}}, \tag{7}$$

where $[\mu/\rho]_{t_i}$ are the mass attenuation coefficients measured using wafers of different thicknesses $t_i$, $\overline{[\mu/\rho]}$ is the weighted average of $[\mu/\rho]_{t_i}$, and $\sigma_i$ are the corresponding statistical errors in the measurements of $[\mu/\rho]_{t_i}$.

Between 5.0 keV and 5.6 keV, the values of $[\mu/\rho]$ are corrected for harmonic contamination as discussed in Sec. VI. In this energy range, the final uncertainty $\sigma_{[\mu/\rho]}$ is the root mean square of the contributions of $\sigma_t$ and of the final error in the procedure of the harmonic correction $\sigma_{har}$, with the later calculated from

$$\sigma_{har}=\sqrt{\sigma_{fit}^2+\sigma_{stat}^2}, \tag{8}$$

where $\sigma_{fit}$ is the fitting error and $\sigma_{stat}$ is the minimum of the statistical errors $\sigma_i$.

Mass attenuation coefficients and their uncertainties are not affected by the value of the density. It is for this reason that the mass attenuation coefficient $[\mu/\rho]$ rather than the linear attenuation coefficient $\mu$ should be used for comparisons of data from different sources.

### B. Summary of uncertainties

Table II summarizes the major sources of uncertainty contributing to the final results. Major factors affecting the precision or the consistency of the measurements of $[\mu/\rho]$ using multiple foils are listed in the first part of Table II. Apart from the intrinsic statistics of the system at the level of 0.02%, the other main factors affecting the measurement consistency in this experiment are Bragg diffraction and the harmonic contamination in the low-energy range of the measurements.

Uncertainties from the fitting of the harmonic contamination of the incident beam below 5.6 keV are at the level of 0.3%. In the high-energy range, measurements that were significantly affected by Bragg diffraction (whose measured $[\ln(I/I_0)]$ were more than 0.5% higher than those from the other two specimens) were excluded from the calculations of the final results. The remaining points were consistent to better than 0.44% (maximum discrepancy at 18.226 keV as listed in Table I).

Uncertainties in the correction of the backlash hysteresis of the monochromator amounted to 1.3 eV or less between 5 keV and 6 keV. The effect of hysteresis is thus less than 0.07% in $[\mu/\rho]$ in this energy range. Errors in the energy determination of less than 1 eV elsewhere are equivalent to less than 0.01% in $[\mu/\rho]$.

These main components affecting the experimental precision resulted in the final experimental precision listed in the second group of Table II. This contributed to the total experimental accuracy at levels of 0.3% below 5.6 keV and up to 0.44% in the higher-energy region.

Uncertainty from the determination of the thicknesses of the specimens increased from 0.06% (at 20 keV) to 0.139% (at 5 keV) due to the additional contribution from the thickness transfer procedure discussed in Ref. [23]. Mika *et al.* [13] and Gerward [10] reported similar accuracies [3 $\mu$m

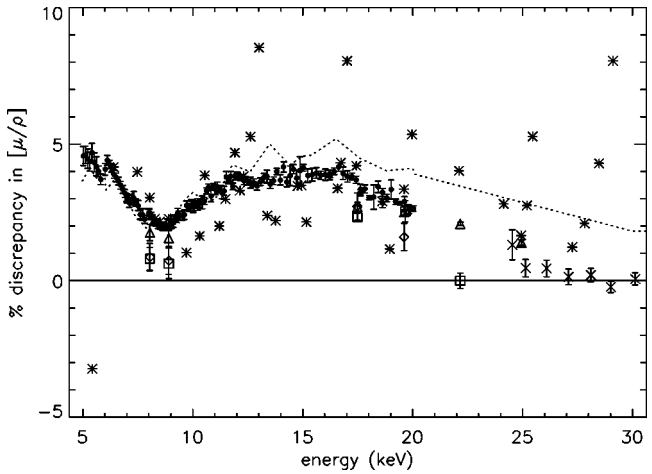


FIG. 7. Discrepancies in the total cross section of silicon between experiments from Gerward [10] (diamonds), Wang *et al.* [14] (asterisks), Creagh and co-workers [11,12] (squares), Baltazar-Rodrigues and Cusatis [15] (triangles), Mika *et al.* [13] (crosses) and this work (circles); and theories from Chantler [16] (solid line) and XCOM [18] (dashed line). Predictions from the nonrelativistic Hartree-Fock-Slater model (XCOM) are higher than those from the relativistic Dirac-Hartree-Fock (Chantler). Theoretical predictions of the total cross sections are the sum of the photoelectric, the Compton, and the TDS components. For further discussion see the text.

(0.075%) and 2 $\mu$m (0.05%), respectively] for specimens of similar (4 mm) thickness. However, their results were for the local thickness measured with a micrometer and not for the absolute accuracy of the determination. Baltazar-Rodrigues *et al.* [15] reported 0.3 $\mu$m accuracy in the thickness determination of their silicon specimens between 100 $\mu$m and 800 $\mu$m but they appear to have used the average thicknesses of the specimens. Both methods (micrometry and average thickness) differ from the local mass per unit area actually seen by the x-ray beam and determined by our technique. The error can be significant as discussed elsewhere [23].

## IX. COMPARISON OF RESULTS WITH THEORY

Figure 7 is a plot of the percent discrepancy between the theoretical precisions of the nonrelativistic Hartree-Fock-Slater model of Scofield [17] used by Berger and Hubbell in XCOM [18] referred to the relativistic Dirac-Hartree-Fock calculation of Chantler [16]. Also plotted is the percent discrepancy between the mass attenuation coefficients measured by various authors and Chantler's calculated values. The theoretically calculated values include Compton and TDS scattering and are thus directly comparable with the measured mass attenuation coefficients.

Between 20 keV and 25 keV there is very little consistent experimental data. Theoretical computations have quoted uncertainties of 1% or more, so the separation of the two models plotted is only $1\sigma$–$3\sigma$ across the plotted energy range. Our experimental data has much smaller error bars. Other experimental points have large error bars (e.g., Wang *et al.* [14] has $\sigma = 1-4\%$ and a scatter greater than this), as shown in Fig. 1 but omitted in Fig. 7 to demonstrate the trend and precision of our data compared to the scatter of earlier work. Some of the best earlier data lies between both models and is moderately consistent with both the experimental results of this work and with both alternate theoretical computations. These earlier experimental results therefore do not discriminate between the different theoretical approaches.

As seen from the figure, in the lower-energy region the discrepancies of our measured mass attenuation coefficients are remarkably close to those from XCOM and reproduce some of the structure in the XCOM discrepancy. As the energy approaches 20 keV, the discrepancy between our measured mass attenuation coefficients and Chantler's calculation appears to diminish.

The trend of our data appears, moreover, to be picked up by the measurements of Mika *et al.* [13] and between 25 keV and 33 keV these results are in very good agreement with Chantler's calculations. Between 33 keV and 50 keV the experimental results of Mika *et al.* fall below the Chantler values, while remaining within $1\sigma$. With increasing energies the relative contributions of Compton and TDS scattering increase, reaching 50% and 25% of the photoelectric component at 50 keV. Errors in the theoretical calculation of scattering therefore become increasingly important and could easily account for the residual discrepancy between the experimental results and the calculated values of Chantler.

The lack of measurements in the gap between our results and those of Mika *et al.* is rather unfortunate and reliable measurements in this energy region would thus be quite important.

In view of the disagreement of the measured and calculated mass attenuation coefficients, renewed consideration needs to be given to the modelling of the nuclear amplitude, electron correlation effects and the calculation of Compton and TDS contributions. The electron correlation and coupling effects, are strongly energy dependent and a more sophisticated modeling of these may well be required to account for present inconsistencies between theory and experiment.

It is interesting to compare our measurements with those for copper (Ref. [20], Fig. 8) where, outside the absorption-edge affected region, there was good agreement with the results of both Chantler and XCOM, the two computations being in reasonable agreement.

## X. CONCLUSION

It has been shown that by using the x-ray extended range technique one can achieve consistent measurements of the absolute mass attenuation coefficients as a function of energy. The level of accuracy and precision attained has enabled us to compare our results with two theoretical calculations and to raise some questions about the modeling used. Further experimental work in the energy range between 20 keV and 25 keV, in particular, is required to investigate the consistency (or inconsistency) between this work and Mika *et al.* [13], and their comparison with theory.

[1] P.S. Peercy, Nature (London) **406**, 1023 (2000).
[2] P.J. Mohr and B.N. Taylor, Rev. Mod. Phys. **72**, 351 (2000); P.J. Mohr and B.N. Taylor, J. Phys. Chem. Ref. Data **28**, 1713 (1999).
[3] R.D. Deslattes and A. Henins, Phys. Rev. Lett. **31**, 972 (1973); R.D. Deslattes, M. Tanaka, G.L. Greene, A. Henins, and E.G. Kessler, Jr., IEEE Trans. Instrum. Meas. **36**, 166 (1987).
[4] W. Parrish, A.J.C. Wilson, and J.I. Langford, in *International Tables for X-ray Crystallography*, edited by A.J.C. Wilsons and E. Prince (Kluwer Academic, Dordrecht, 1999), Vol. C, Sec. 5.2.10.
[5] J. Li, D. Stein, C. McMullan, D. Branton, M.J. Aziz, and J.A. Golovchenko, Nature (London) **412**, 166 (2001).
[6] M. Gratzel, Nature (London) **414**, 338 (2001).
[7] K-D. Liss, R. Hock, M. Gomm, B. Waibel, A. Magerl, M. Krisch, and R. Tucoulou, Nature (London) **404**, 371 (2000).
[8] B. Koiller, Xuedong Hu, and S. Das Sarma, Phys. Rev. Lett. **88**, 027903 (2002).
[9] C.T. Chantler and Z. Barnea, J. Phys.: Condens. Matter **11**, 4087 (1999).
[10] L. Gerward, J. Phys. B: At., Mol. Phys. **14**, 3389 (1981).
[11] D.C. Creagh and J.H. Hubbell, Acta Crystallogr., Sect. A: Found. Crystallogr. **43**, 102 (1987).
[12] D.C. Creagh, Nucl. Instrum. Methods Phys. Res. A **255**, 1 (1987).
[13] J.F. Mika, L.J. Martin, and Z. Barnea, J. Phys. C **18**, 5215 (1985).
[14] Wang Da-Chun, Luo Ping-An, and Yang Hua, Nucl. Instrum. Methods Phys. Res. B **95**, 161 (1995).
[15] J. Baltazar-Rodrigues and C. Cusatis, Nucl. Instrum. Methods Phys. Res. B **179**, 325 (2001).
[16] C.T. Chantler, J. Phys. Chem. Ref. Data **22**, 71 (1995); **29**, 597 (2000).
[17] J.J. Scofield, LLNL Report No. UCRI-51326, 1973 (unpublished).
[18] M.J. Berger and J.H. Hubbell, Report No. NBSIR 87-3597, XCOM: Photo cross sections on a personal computer, 1987 (unpublished).
[19] C.T. Chantler, C.Q. Tran, D. Paterson, D. Cookson, and Z. Barnea, Phys. Lett. A **286**, 338 (2001).
[20] C.T. Chantler, C.Q. Tran, Z. Barnea, D. Paterson, D.J. Cookson, and D.X. Balaic, Phys. Rev. A **64**, 062506 (2001).
[21] C.Q. Tran, Ph.D. thesis, University of Melbourne, 2002 (unpublished).
[22] J.S. Coursey, D.J. Schwab, and R.A. Dragoset, Atomic Weights and Isotopic Compositions (version 2.3.1), http://physics.nist.gov/Comp, NIST, Gaithersburg, MD 20899; T.B. Coplen, Pure Appl. Chem. **73**, 667 (2001); K.J.R. Rosman and P.D.P. Taylor, J. Phys. Chem. Ref. Data **27**, 1275 (1998); P.J. Mohr and B.N. Taylor, *ibid.* **28**, 1713 (1999); Rev. Mod. Phys. **72**, 351 (2000).
[23] C.Q. Tran, M. de Jonge, C.T. Chantler, and Z. Barnea (unpublished).
[24] J.H. Hubbell, W.J. Veigele, E.A. Briggs, R.T. Brown, D.T. Cromer, and R.J. Howerton, J. Phys. Chem. Ref. Data **4**, 471 (1975).
[25] Z. Barnea, R. Clapp, D.C. Creagh, T.M. Sabine, A.W. Stevenson, J.W. White, S.W. Wilkins, J. Harada, H. Hashizume, Y. Kashihara, M. Sakata, K. Ohsumi, and T. Zemb, Rev. Sci. Instrum. **60**, 2537 (1989).
[26] Z. Barnea, D.C. Creagh, T.J. Davis, R.F. Garrett, S. Janky, A.W. Stevenson, and S.W. Wilkins, Rev. Sci. Instrum. **63**, 1069 (1992).
[27] T.M. Sabine, B.J. Kennedy, R.F. Garrett, G.J. Foran, and D.J. Cookson, J. Appl. Crystallogr. **28**, 513 (1995).
[28] C.T. Chantler, C.Q. Tran, D. Paterson, Z. Barnea, and D.J. Cookson, X-Ray Spectrom. **29**, 449 (2000).
[29] C.T. Chantler, C.Q. Tran, D. Paterson, Z. Barnea, and D.J. Cookson, X-Ray Spectrom. **29**, 459 (2000).
[30] C.Q. Tran, Z. Barnea, M. de Jonge, B.B. Dhal, D. Paterson, D. Cookson, and C.T. Chantler, X-Ray Spectrom. **32**, 69 (2003).
[31] L. Gerward, G. Thuesen, M.S. Jensen, and I. Alstrup, Acta Crystallogr., Sect. A: Cryst. Phys., Diffr., Theor. Gen. Crystallogr. **35**, 852 (1979).
[32] P.F. Price, E.N. Maslen, and S.L. Mair, Acta Crystallogr., Sect. A: Cryst. Phys., Diffr., Theor. Gen. Crystallogr. **34**, 183 (1978).
[33] E.N. Maslen, A.G. Fox, and M.A. O'Keefe, in *International Tables for Crystallography*, edited by A.J.C. Wilson and E. Prince, 2nd ed. (Kluwer Academic, Dordrecht, 1999), Vol. C, Sec. 6.1.1, Table 6.1.1.4.